

A physically based model for bcc materials including non-Schmid effects and its application to single crystals of α -iron at different model scales

Mohammad Hasan Joudivand S.^{a,b}, Eralp Demir^{a,b,*}

^a*Faculty of Engineering and Natural Sciences, Sabanci University, 34956 Tuzla, Istanbul, Turkey*

^b*Integrated Manufacturing Technologies Research and Application Center, Sabanci University, 34956 Tuzla, Istanbul, Turkey*

Abstract

A dislocation density based model is developed to govern physics of complex mechanical behavior of bcc materials. Non-Schmid effects are incorporated into a novel dislocation density based model by using three-term projection operators. The model is used to explain dependence of mechanical response to crystal orientation, temperature, strain-rate and as well as tension-compression asymmetry. Simulations at different scales that include; a material point, a single finite element and a finite element model of exact test geometry were performed. The proposed model successfully captures crystal orientation, temperature, and strain-rate dependence of the experimentally observed stress-strain curves and also well explain the tension-compression asymmetry of experimental flow stresses of α -iron. The forest projection scheme that uses the slip plane normal, hardening interactions between slip systems for bcc materials, non-Schmid projections, and Peierls energy barrier for thermal activation of slip were important features of the model to imitate experimental mechanical behavior of bcc materials successfully at all scales with a better agreement though a finite element model considering exact tensile specimen geometry.

Keywords: crystal plasticity, single crystal, bcc, physics based modeling, Non-Schmid

*Corresponding author

Email address: eralp.demir@sabanciuniv.edu (Eralp Demir)

effects, forest projections

1. Introduction

Single crystal deformation must be well understood in order to model the mechanical behavior of polycrystalline materials with complex microstructure. Many of the widely used single or multi-phase metals (i.e. steel, silicon, tantalum etc.) have bcc crystal structure. Therefore, there is a great demand to develop physics based models that have inherent temperature, strain-rate and crystal orientation dependence of bcc materials for accurate prediction of mechanical behavior of single and polycrystal materials as highlighted in the recent studies [1, 2, 3].

In bcc materials, slip is along specific closed packed crystallographic family of $\langle 111 \rangle$ directions, but on various glide planes that is referred as pencil glide. Experimental observations suggested the crystallographic family of slip planes were $\{110\}$, $\{112\}$, and $\{123\}$ as the active for a wide range of temperatures, that makes 48 number of slip systems in total [4]. Commonly observed active slip planes for bcc materials at room temperature were $\{110\}$ and $\{112\}$ [5, 6, 7, 8, 9, 10, 11, 12, 13, 14].

In bcc metals, deformation is governed by lattice friction rather than obstacle resistance in fcc metals [15]. The motion of screw dislocations determines the plastic strain rate in bcc materials since edge dislocations move relatively faster than the screw dislocations that move in the form of double kinks. Therefore, Peierls stress threshold was incorporated to physics based models as a thermally activated barrier in earlier studies [16]. The motion of screw dislocations control the flow stress in bcc metals hence relevant screw dislocation kinetics were used to determine the yield point at different hardening stages [17].

Mechanical tests on single crystals of bcc showed significant deviations from Schmid Law [18]. Schmid Law states that the active slip systems are the ones that possess the highest resolved shear stresses (RSS) which makes them critical plane-direction combinations

[19]. The rate of deformation and temperature were the two major factors that significantly influence the deformation behavior of bcc materials [20, 21]. Experiments on high-purity single crystals of Molybdenum [22, 23] and Niobium [24, 25, 9] at low-temperature under tension and compression loads showed significantly different stress-strain behavior that was dependent on the temperature. This behavior was attributed to the spatial spread of screw dislocation core [26]. The phenomenon addresses the glide of the dislocations with lower resolved shear stress (break-down of the Schmid law) through the stresses acting on the secondary conjugated planes [27]. In addition, the experiments on bcc single crystals for different crystal orientations revealed the effect of non-glide shear stresses. Accordingly, atomistic simulations of motion of screw dislocations in bcc crystals showed that screw dislocations were not confined to their slip planes but decompose into several planes normal to the $\langle 111 \rangle$ slip direction, the most significant of which were found to be $\{110\}$ family of planes [28, 29, 30, 26]. Dislocation activity in the bcc structure were influenced by the other stress components than the Schmid stresses. Therefore, the mechanical behavior of a bcc crystal was highly dependent on the crystallographic orientation with respect to the load as well as the type of the load, whether it is compression or tension.

BCC crystal structure and its geometry was investigated to better understand the deformation and correlate the applied stress to the deformation [13, 27, 31, 32, 33, 34]. Comparison of bcc material behavior on crystal orientations for different materials revealed that the behavior of screw dislocations depends on the normal stress components perpendicular to the slip direction [35] as well as shear or Schmid stresses. The effective three parameter laws were derived for $\{110\}$ crystallographic family of slip planes. For this reason, the three non-Schmid terms were incorporated into crystal plasticity models to better represent tension-compression asymmetry and crystal orientation dependence of bcc metals [36].

Dislocation density based models have been used to better represent the temperature dependent physics of the plasticity of metals [37, 38, 39, 40, 41, 42, 43, 44]. Dislocation

density based model allowed better representation of dislocation kinetics such as Orowan law, thermally activated slip, or Peierls barrier. In addition, better hardening response was obtained by using a dislocation interaction matrix that considers the dominant dislocation reactions between the slip systems [45, 46, 47, 48]. Therefore, physics based relations have started to become more popular to express polycrystal response or deformation behavior of a single crystal with a complicated loading state such as indentation.

Crystal plasticity models were used to predict non-Schmid effects and yield behavior of the bcc single crystals. Accordingly, Qin and Bassani suggested to incorporate the influence of non-glide stresses as a phenomenological way in the flow rule through introducing effective yield stress as the non-Schmid contribution term [49, 50]. Similarly, Steinmann et al. pioneered the use of two additional non-Schmid terms as projections to the slip plane normal and projection to the co-slip direction [51]. Yalcinkaya et al. used a physics based thermal activation models [52] for material point simulations by including twinning and anti-twinning asymmetry with the slip plane families of $\{110\}$ and $\{112\}$ [53]. Crystal plasticity constitutive models, that incorporate the non-Schmid terms of $\{110\}$ slip plane family separately for positive and negative slip directions by three non-Schmid terms [17, 54], were used to relate the crystal orientation dependence of the critical resolved shear stress. Recently, polycrystal simulations were performed for combined effect of non-Schmid terms and crystallographic texture considering three and five parameter non-Schmid terms [55].

In this work, a unique physics based crystal plasticity model is developed to deal with Schmid and non-Schmid features of bcc materials. The yield behavior of bcc single crystal is governed by a single state variable as the dislocation density that is used to derive the remaining properties (i.e. mobile dislocation density, dislocation evolution rates, slip rates, etc.). Non-Schmid effects are incorporated to the model by using three non-Schmid parameters as a result of dislocation based simulations by considering only $\{110\}$ family of crystallographic planes [17]. The proposed physics based model is used to simulate the avail-

able experimental and numerical literature findings for bcc single crystals of α -iron at three different modeling scales as the material point (MP), single finite element (SE) and exact test geometry (ETG) that consists of multiple number of finite elements. Effects of the crystallographic orientation, strain rate and temperature dependence on the stress-strain response (yield, hardening behavior, and tension/compression asymmetry) of bcc single crystals are investigated in a comprehensively by using the proposed model.

2. Model

Section 2.1 explains the crystal plasticity kinematics including non-Schmid feature inherent to bcc materials. Section 2.2 shows the unique combination of physically based constitutive relations that are used to relate mechanical properties to crystal orientation, temperature and strain-rate. Section 3 presents the model results and discussion that compares the model results with the experimental findings in the literature for single crystal α -iron. Finally, Section 4 shows the conclusions.

2.1. Crystal mechanics

The total deformation gradient¹, \mathbf{F} , is ideally multiplicatively decomposed into its elastic, \mathbf{F}_e , and plastic, \mathbf{F}_p , parts in Equations (1), as described in [56]. Crystal plasticity problem is about to identification of how much of the deformation is elastic or plastic for a prescribed total deformation.

$$\mathbf{F} = \mathbf{F}_e \mathbf{F}_p \quad (1)$$

The Green-Lagrange strain measure is used to find the elastic strains, \mathbf{E}_e , for large

¹Upper and lower case bold letters are used to indicate second order tensors and vectors, respectively ($\mathbf{A} = A_{ij}$, $\mathbf{b} = b_i$). Letters in regular font indicate scalars. The symbol $:$ represents the inner product ($\mathbf{A} : \mathbf{A} = A_{ij} A_{ij}$). \mathbf{I} refers to the three by three identity matrix. The superscript T denotes transpose.

deformations as in Equation (2).

$$\mathbf{E}_e = \frac{\mathbf{F}_e^T \mathbf{F}_e - \mathbf{I}}{2} \quad (2)$$

The vectorized form of the stress driving the dislocation glide in the intermediate configuration (2nd Piola-Kirchhoff stress), $\boldsymbol{\sigma}$, is calculated using the elasticity. In Equation (3), \mathbf{e}_e and \mathbf{C} are the vectorized form of the elastic strain and the elasticity matrix, respectively.

$$\boldsymbol{\sigma} = \mathbf{C} \cdot \mathbf{e}_e \quad (3)$$

Further, \mathbf{C} is the elasticity matrix in the crystal frame that is constructed using three temperature-dependent elastic constants for cubic metals; C_{11} , C_{12} , and C_{44} as in Equation (4).

$$\mathbf{C} = \begin{bmatrix} C_{11} & C_{12} & C_{12} & 0 & 0 & 0 \\ C_{12} & C_{11} & C_{12} & 0 & 0 & 0 \\ C_{12} & C_{12} & C_{11} & 0 & 0 & 0 \\ 0 & 0 & 0 & C_{44} & 0 & 0 \\ 0 & 0 & 0 & 0 & C_{44} & 0 \\ 0 & 0 & 0 & 0 & 0 & C_{44} \end{bmatrix} \quad (4)$$

The resolved shear stress, τ^α , is obtained by projection of the 2nd Piola-Kirchhoff stress, $\boldsymbol{\sigma}$, to the slip system α using the Schmid tensor, \mathbf{S}^α using Equation (5).

$$\tau^\alpha = \mathbf{F}_e^T \mathbf{F}_e \boldsymbol{\sigma} : \mathbf{S}^\alpha \quad (5)$$

Schmid tensor, \mathbf{S}^α , is the dyadic product of slip direction, \mathbf{s}^α , and slip plane normal, \mathbf{n}^α

Table 1: Slip vectors in the crystal reference frame for bcc materials. \mathbf{s}^α and \mathbf{n}^α denote slip directions and slip plane normals that are $\langle 111 \rangle$ family of directions and $\{110\}$ family of planes, respectively. \mathbf{n}_1^α that are used to compute the non-Schmid stresses leading to the tension-compression asymmetry.

slip sys. (Schmid Boas)	\mathbf{s}^α	\mathbf{n}^α	\mathbf{n}_1^α	slip sys.	\mathbf{s}^α	\mathbf{n}^α	\mathbf{n}_1^α
1 (B2)	$[1\ 1\ 1]$	$(0\ 1\ \bar{1})$	$(\bar{1}\ 1\ 0)$	13	$[\bar{1}\ \bar{1}\ \bar{1}]$	$(0\ 1\ \bar{1})$	$(1\ 0\ \bar{1})$
2 (B4)	$[1\ 1\ 1]$	$(\bar{1}\ 0\ 1)$	$(0\ \bar{1}\ 1)$	14	$[\bar{1}\ \bar{1}\ \bar{1}]$	$(\bar{1}\ 0\ 1)$	$(\bar{1}\ 1\ 0)$
3 (B5)	$[1\ 1\ 1]$	$(1\ \bar{1}\ 0)$	$(1\ 0\ \bar{1})$	15	$[\bar{1}\ \bar{1}\ \bar{1}]$	$(1\ \bar{1}\ 0)$	$(0\ \bar{1}\ 1)$
4 (A3)	$[\bar{1}\ 1\ 1]$	$(\bar{1}\ 0\ \bar{1})$	$(\bar{1}\ \bar{1}\ 0)$	16	$[1\ \bar{1}\ \bar{1}]$	$(\bar{1}\ 0\ \bar{1})$	$(0\ 1\ \bar{1})$
5 (A2)	$[\bar{1}\ 1\ 1]$	$(0\ \bar{1}\ 1)$	$(1\ 0\ 1)$	17	$[1\ \bar{1}\ \bar{1}]$	$(0\ \bar{1}\ 1)$	$(\bar{1}\ \bar{1}\ 0)$
6 (A6)	$[\bar{1}\ 1\ 1]$	$(1\ 1\ 0)$	$(0\ 1\ \bar{1})$	18	$[1\ \bar{1}\ \bar{1}]$	$(1\ 1\ 0)$	$(1\ 0\ 1)$
7 (C1)	$[\bar{1}\ \bar{1}\ 1]$	$(0\ \bar{1}\ \bar{1})$	$(1\ \bar{1}\ 0)$	19	$[1\ 1\ \bar{1}]$	$(0\ \bar{1}\ \bar{1})$	$(\bar{1}\ 0\ \bar{1})$
8 (C3)	$[\bar{1}\ \bar{1}\ 1]$	$(1\ 0\ 1)$	$(0\ 1\ 1)$	20	$[1\ 1\ \bar{1}]$	$(1\ 0\ 1)$	$(1\ \bar{1}\ 0)$
9 (C5)	$[\bar{1}\ \bar{1}\ 1]$	$(\bar{1}\ 1\ 0)$	$(\bar{1}\ 0\ \bar{1})$	21	$[1\ 1\ \bar{1}]$	$(\bar{1}\ 1\ 0)$	$(0\ 1\ 1)$
10 (D4)	$[1\ \bar{1}\ 1]$	$(1\ 0\ \bar{1})$	$(1\ 1\ 0)$	22	$[\bar{1}\ 1\ \bar{1}]$	$(1\ 0\ \bar{1})$	$(0\ \bar{1}\ \bar{1})$
11 (D1)	$[1\ \bar{1}\ 1]$	$(0\ 1\ 1)$	$(\bar{1}\ 0\ 1)$	23	$[\bar{1}\ 1\ \bar{1}]$	$(0\ 1\ 1)$	$(1\ 1\ 0)$
12 (D6)	$[1\ \bar{1}\ 1]$	$(\bar{1}\ \bar{1}\ 0)$	$(0\ \bar{1}\ \bar{1})$	24	$[\bar{1}\ 1\ \bar{1}]$	$(\bar{1}\ \bar{1}\ 0)$	$(\bar{1}\ 0\ 1)$

of slip system α , Equation (6).

$$\mathbf{S}^\alpha = \mathbf{s}^\alpha \otimes \mathbf{n}^\alpha \quad (6)$$

Table 1 shows the list of the slip plane normals and the slip directions for bcc materials that are taken from the reference [40]. Only one slip plane family of $\{110\}$ is assumed to be active and the slip is considered along positive and negative slip directions separately thereby giving 24 possible slip systems in total.

The plastic flow rule from kinematics is governed by Equation (7).

$$\dot{\mathbf{F}}_{\mathbf{p}} = \mathbf{L}_{\mathbf{p}} \mathbf{F}_{\mathbf{p}} \quad (7)$$

The plastic velocity gradient, $\mathbf{L}_{\mathbf{p}}$, is obtained by summing up the plastic slip rates, $\dot{\gamma}^\alpha$, at each slip systems, Equation (8).

$$\mathbf{L}_{\mathbf{p}} = \sum_{\alpha=1}^{24} \tilde{\mathbf{S}}^\alpha \dot{\gamma}^\alpha \quad (8)$$

Cauchy stress, the stress at the deformed configuration, $\tilde{\sigma}$, is computed using Equation (9).

$$\tilde{\sigma} = \mathbf{F}_e \boldsymbol{\sigma} \mathbf{F}_e^T / \det(\mathbf{F}_e) \quad (9)$$

The three terms in Equation (10) to collectively represent the non-Schmid effects. a_1 , a_2 , and a_3 are the constants.

$$\sigma_{ns}^\alpha = [a_1 \mathbf{s}^\alpha \otimes \mathbf{n}_1^\alpha + a_2 (\mathbf{n}^\alpha \times \mathbf{s}^\alpha) \otimes \mathbf{n}^\alpha + a_3 (\mathbf{n}_1^\alpha \times \mathbf{s}^\alpha) \otimes \mathbf{n}_1^\alpha] : \boldsymbol{\sigma} \quad (10)$$

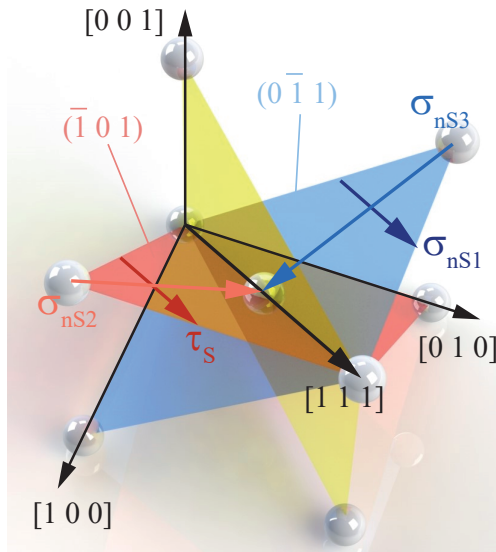


Figure 1: Schematic sketch of Schmid and non-Schmid projections for bcc crystal structure. Example illustration is shown for slip system $\alpha = 2$ or B4 in Schmid-Boas notation. The vectors that belong the same plane are indicated with the same color of the plane.

Figure 1 shows the directions and planes of three non-Schmid terms for an example case (slip system $\alpha = 2$ or B4) as shown in the reference [57]. The three non-Schmid terms are described as follows:

- $\sigma_{ns1}^\alpha = \mathbf{s}^\alpha \otimes \mathbf{n}_1^\alpha : \boldsymbol{\sigma}$ – Stress component parallel to slip direction and on the plane with 60° to the glide plane (non-Schmid term for Twinning/Anti-Twinning asymmetry)
- $\sigma_{ns2}^\alpha = (\mathbf{n}^\alpha \times \mathbf{s}^\alpha) \otimes \mathbf{n}^\alpha : \boldsymbol{\sigma}$ – Stress component normal to the slip direction on the

slip plane (non-Schmid term for Tension/Compression asymmetry)

- $\sigma_{ns3}^\alpha = (\mathbf{n}_1^\alpha \times \mathbf{s}^\alpha) \otimes \mathbf{n}_1^\alpha : \boldsymbol{\sigma}$ – Stress component normal to the slip direction on the plane with 60° to the glide plane (non-Schmid term for Tension/Compression asymmetry)

The effective shear stress on the slip system α , τ_{eff}^α , is obtained by adding the non-Schmid component of the stress, σ_{ns}^α , to the resolved shear stress (Schmid term) and by subtracting the effect of long-rang stresses, Equation (11).

$$\tau_{eff}^\alpha = \tau^\alpha + \sigma_{ns}^\alpha - \tau_\mu^\alpha \quad (11)$$

The two-level semi-implicit time integration method developed by Dawson et al. [58] is implemented. The method works on the principle for a plastic initial guess which results in more stable converging results than the stress guess based numerical methods [59]. A detailed summary of the numerical solution procedure was explained in [60].

2.2. Dislocation-density-based constitutive laws

In this section, the single-crystal dislocation-density-based constitutive laws are explained. The state variable other than stress per slip system is the single dislocation density at the slip system α , ϱ^α . All the other constitutive quantities are derived using this single state variable per slip system.

The dislocations piercing through the slip plane are referred to as forest dislocations, which have a density of ϱ_f^α . Forest dislocation density is calculated using the projection of slip plane normals, that is a unique feature of this study, Equation (12).

$$\varrho_f^\alpha = \sum_{\beta=1}^{24} (1 - \mathbf{n}^\alpha \cdot \mathbf{n}^\beta) \varrho^\beta \quad (12)$$

2.2.1. Dislocation kinetics

The rate form of the Orowan equation is used to find the shear rates on the slip systems, $\dot{\gamma}^\alpha$. In Equation (13), b , ϱ_m^α , and v^α are the Burgers vector, mobile dislocation density, and average glide velocity, respectively [61].

$$\dot{\gamma}^\alpha = \varrho_m^\alpha b v^\alpha \quad (13)$$

The average glide velocity, v^α , is computed by the geometric average velocities of viscous drag, v_{dr}^α , and thermal activation, v_{th}^α , Equation (14) [43].

$$\frac{1}{v^\alpha} = \frac{1}{v_{dr}^\alpha} + \frac{1}{v_{th}^\alpha} \quad (14)$$

The thermally activated velocity is a function of the work done by the applied effective stress, τ_{eff}^α , over an existing long range athermal stress field, τ_μ^α , to pass short range obstacles that is the Peierls barrier for bcc metals. In Equation (15), Q_{Pei} , K_B , T , ν_0 , d^α , and V^α refer to Peierls activation energy, Boltzmann constant, temperature, Debye frequency, jump distance, and activation volume, respectively. The direction of effective stress and shear stress shall be always positive since negative slip systems are accounted [15].

$$v_{th}^\alpha = \begin{cases} \nu_0 d^\alpha \exp\left(-\frac{Q_{Pei}}{K_B T}\right) \exp\left(\frac{\tau_{eff}^\alpha V^\alpha}{K_B T}\right), & \text{if } (\tau_{eff}^\alpha > 0) \ \& \ (\tau^\alpha > 0). \\ 0, & \text{otherwise.} \end{cases} \quad (15)$$

The temperature and rate-independent part of the flow stress (athermal) contributes as the long-range part of the flow stress, τ_μ^α . The temperature dependence of τ_μ^α is only due to the temperature dependence of the shear modulus, G [62]. The long-range internal stress fields extend over a long distance such that the effect of thermal fluctuations is negligible. The athermal part of the flow stress, τ_μ , is computed by Equation (16) in which c_1 is the

geometric factor and ϱ^α refers to the density of primary dislocations.

$$\tau_\mu^\alpha = c_1 G b \sqrt{\varrho^\alpha} \quad (16)$$

The obstacle-free distance for a dislocation line or jump distance, d^α , is inversely proportional to the square root of the forest dislocation density, as shown in Equation (17) in which c_2 is the scaling constant [62, 61].

$$d^\alpha = \frac{c_2}{\sqrt{\varrho_f^\alpha}} \quad (17)$$

The activation volume, V^α , is proportional to b^3 and constant c_3 as in Equation (18) [4].

$$V^\alpha = c_3 b^3 \quad (18)$$

The drag velocity in Equation (14) is computed as linear function of the effective stress, Equation (19) [43].

$$v_{dr}^\alpha = \frac{b \tau_{eff}^\alpha}{B_0} \quad (19)$$

B_0 is the drag constant that is computed from Equation (20) in which q , c_s and b represent the number of atoms per unit cell (two for bcc materials), and shear wave speed. Shear wave speed is calculated using shear modulus, G , and mass density, ρ , using $c_s = \sqrt{G/\rho}$.

$$B_0 = \frac{3 K_B T q}{20 c_s b^2} \quad (20)$$

Mobile dislocation density ϱ_m^α is a fraction of the overall dislocation density [15], $r(\tau^\alpha, \varrho_f^\alpha)$, Equation (21).

$$\varrho_m^\alpha = r(\tau^\alpha, \varrho_f^\alpha) \varrho^\alpha \quad (21)$$

Mobile dislocation density is calculated by assuming a simplified form of log-normal dis-

tribution based on the mean spacing of dislocation. The critical bow-out radius is computed using the applied effective stress. The segments that are longer than the critical bow out radius are assumed mobile [47], Equation (22).

$$r(\tau^\alpha, \varrho_f^\alpha) = c_7 (2\pi)^{3/2} \left(\frac{\tau^\alpha}{Gb}\right)^2 \frac{1}{\varrho_f^\alpha} \quad (22)$$

2.2.2. Dislocation evolution

The dislocations are stored after traveling a distance of mean-free-path that is inversely proportional to the square root of the dislocation density [62]. The increase in the dislocation density, $\dot{\varrho}_{mul}^\alpha$, due to multiplication of dislocations is computed by Equation (23).

$$\dot{\varrho}_{mul}^\alpha = c_4 \frac{\sqrt{\varrho^\alpha}}{b} |\dot{\gamma}^\alpha| \quad (23)$$

Dipole formation is another dislocation storage mechanism for mobile dislocations, $\dot{\varrho}_{dip}^\alpha$. The storage rate was related to inverse of the applied stress in former references [46]. In Equation (24), ν is the Poisson ratio.

$$\dot{\varrho}_{dip}^\alpha = c_8 \frac{\sqrt{3} G b \varrho_m^\alpha}{16 \pi (1 - \nu) \tau_{eff}^\alpha} |\dot{\gamma}^\alpha| \quad (24)$$

Dislocation climb is a high temperature dislocation annihilation reaction, $\dot{\varrho}_{climb}^\alpha$. Climb rate is assumed to be a function of climb stress, σ^α , effective diffusion rate, D_{eff} as shown in Equation (25) according Frost and Ashby [63]. $c_5 b$ represents the climb distance that is an integer multiple of Burgers vector.

$$\dot{\varrho}_{climb}^\alpha = -c_5 \frac{D_{eff} b^3 \sigma^\alpha}{2 K_B T} (\varrho^\alpha)^2 |\dot{\gamma}^\alpha| \quad (25)$$

The effective rate of climb, D_{eff} , is related to volume diffusion and core diffusion with

coefficients of D_v and $a_c D_c$, respectively with Equation (26).

$$D_{eff} = D_v + \varrho^\alpha a_c D_c \quad (26)$$

The diffusion rate terms are related to climb activation energies of Q_v and Q_c as well as reference volume and core diffusion rates of D_{v0} and $a_c D_{c0}$ as in Equation set (27).

$$\begin{aligned} D_v &= D_{v0} \exp\left(-\frac{Q_v}{K_B T}\right) \\ D_c &= a_c D_{c0} \exp\left(-\frac{Q_c}{K_B T}\right) \end{aligned} \quad (27)$$

Only a few dislocation density models use the force along the slip plane normals as the driving force for dislocation climb [2, 64]. Therefore, the driving stress for climb, σ^α , is along the slip plane normal, not the resolved shear stress as shown in Equation (28).

$$\sigma^\alpha = \mathbf{n}^\alpha \otimes \mathbf{n}^\alpha : \boldsymbol{\sigma} \quad (28)$$

The major dislocation annihilation mechanism for bcc materials is cross-slip, $\dot{\varrho}_{cs}^\alpha$. Bonneville and Escaig thermally activated cross-slip model is used in this model [65] as shown in Equation (29).

$$\dot{\varrho}_{cs}^\alpha = -\frac{2\sqrt{\varrho^\alpha} \nu_0}{c_6^2 b} \exp\left(-\frac{Q_{cs}}{K_B T}\right) \exp\left(\frac{g}{K_B T}\right) |\dot{\gamma}^\alpha| \quad (29)$$

The cross-slip energy barrier, Q_{cs} , and activation energy required for cross-slip, g are computed using Equation (31), χ , in which A and B represent the stacking fault energy of

the material, and two other material constants, respectively.

$$g = \frac{\tau_{eff}^\alpha b}{\chi} [\ln(B G b / \chi)]^{-0.5} \quad (30)$$

$$Q_{cs} = A G b^3 \frac{G b}{\chi} [\ln(B G b / \chi)]^{0.5} \quad (31)$$

The total dislocation density is computed by the sum of all of the reactions, Equation (32).

$$\dot{\rho}^\alpha = \frac{1}{2} \chi_\beta^\alpha (\dot{\rho}_{mul}^\beta + \dot{\rho}_{dip}^\beta + \dot{\rho}_{climb}^\beta + \dot{\rho}_{cs}^\beta) \quad (32)$$

In Equation (32), χ_β^α stands for the dislocation interaction matrix that accounts for the difference in the hardening interactions among the slip systems owing to different lock forming mechanisms [66]. For the overall 24 slip systems, the interaction matrix takes the form in Equation (33).

$$\chi_\beta^\alpha = \begin{bmatrix} X_\beta^\alpha & X_\beta^\alpha \\ X_\beta^\alpha & X_\beta^\alpha \end{bmatrix} \quad (33)$$

The dislocation interaction coefficients $g_{d0}, G_0, g_1, g_2, g_3, g_4$ for 12 slip systems in Equation (34) refer to the self, co-planar, glissile, Hirth lock, and Lomer-Cottrell lock dislocation

interactions with values of 0.0, 1.0, 1.5, 3.2, 2.4, and 1.8, respectively.

$$X_{\beta}^{\alpha} = \begin{bmatrix} gd0 & G0 & G0 & g3 & g1 & g3 & g3 & g3 & g3 & g3 & g3 & g3 \\ G0 & gd0 & G0 & g3 & g1 & g3 & g3 & g3 & g3 & g1 & g1 & g1 \\ G0 & G0 & gd0 & g3 & g1 & g3 & g1 & g1 & g1 & g3 & g3 & g3 \\ g3 & g3 & g3 & gd0 & G0 & G0 & g1 & g1 & g1 & g3 & g3 & g3 \\ g1 & g1 & g1 & G0 & gd0 & G0 & g3 & g3 & g3 & g3 & g3 & g3 \\ g3 & g3 & g3 & G0 & G0 & gd0 & g3 & g3 & g3 & g1 & g1 & g1 \\ g3 & g3 & g1 & g1 & g3 & g3 & gd0 & G0 & G0 & g2 & g2 & g2 \\ g3 & g3 & g1 & g1 & g3 & g3 & G0 & gd0 & G0 & g3 & g3 & g3 \\ g3 & g3 & g1 & g1 & g3 & g3 & G0 & G0 & gd0 & g3 & g3 & g3 \\ g3 & g1 & g3 & g3 & g3 & g1 & g2 & g3 & g3 & gd0 & G0 & G0 \\ g3 & g1 & g3 & g3 & g3 & g1 & g2 & g3 & g3 & G0 & gd0 & G0 \\ g3 & g1 & g3 & g3 & g3 & g1 & g2 & g3 & g3 & G0 & G0 & gd0 \end{bmatrix} \quad (34)$$

Equations (35)-(37) shows the values of cubic elastic constants, C_{11} , C_{12} , and C_{44} for α -iron as a function of temperature, T [67].

$$C_{11} = 239260 - 24520/(\exp(392.03/T) - 1) \text{ [MPa]} \quad (35)$$

$$C_{12} = 135780 - 6550/(\exp(469.65/T) - 1) \text{ [MPa]} \quad (36)$$

$$C_{44} = 120720 - 3500/(\exp(162.9/T) - 1) \text{ [MPa]} \quad (37)$$

The shear modulus, G , and Poisson's ratio, ν , are calculated using the elastic constants from Equations (38) and (39).

$$G = \sqrt{(C_{11} - C_{12})C_{44}/2} \quad (38) \quad \nu = \frac{C_{12}}{C_{11} + C_{12}} \quad (39)$$

Table 2 shows the material constants for single crystal α -iron.

Table 3 shows the model constants that are used in the calibration and their descriptions.

Table 2: Description of constants that are calibrated in this study for different experimental findings.

constant	value	unit	description
b	2.86×10^{-10}	m	Burgers vector [68]
K_B	1.38×10^{-23}	J/K	Boltzmann constant [62]
χ	80×10^{-3}	J/m ²	Stacking fault energy [69]
ρ	7890	kg/m ³	mass density
Q_v	197×10^3	J/mole	Volume (lattice) diffusion energy [63]
Q_c	117×10^3	J/mole	Core diffusion energy [63]
D_{v0}	2×10^{-5}	m ² /s	Volume (lattice) diffusion constant [63]
$a_c D_{c0}$	1.0×10^{-24}	m ⁴ /s	Core diffusion constant [63]
A	5×10^{-4}	-	cross-slip constant-1
B	0.07	-	cross-slip constant-2
ν_0	10^{10}	1/s	attack frequency of dislocations [46]
q	2	-	number of atoms per unit cell
G_0	1	-	Co-directional interaction coefficient [66]
g_1	1.5	-	Co-planar interaction [66]
g_2	3.2	-	Lomer-Cottrell interaction [66]
g_3	2.4	-	Glissile junction [66]
g_4	1.8	-	Hirth-Lock interaction [66]

Table 3: Description and values of constants

constant	unit	description
c_1	-	Geometric constant for the long range flow stress
c_2	-	Jump distance constant
c_3	-	Adjusting parameter for activation volume
c_4	-	Mean-free-path hardening constant
c_5	-	Climb distance factor
c_6	-	Cross-slip dislocation width constant
c_7	-	Scaling constant for mobile dislocation density
c_8	-	Scaling constant for dipole storage
a_1	-	Non-Schmid parameter (1st term)
a_2	-	Non-Schmid parameter (2nd term)
a_3	-	Non-Schmid parameter (3rd term)
ϱ^0	1/m ²	Initial dislocation density
Q_{Pei}	J	Peierls energy barrier

2.3. Numerical modeling

The physically based model is applied and simulations are performed at three different scales; material point (MP), single element (SE) and exact test geometry (ETG) models as shown in Figure 2.

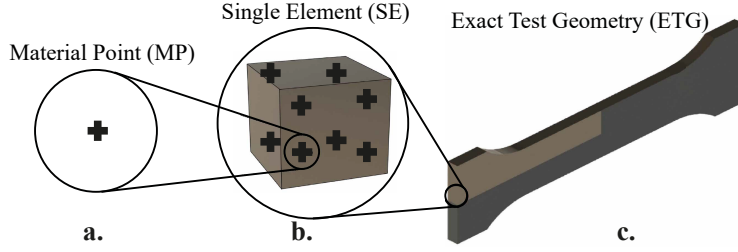


Figure 2: Modeling schemes at different size scales: **a.** material point model (MP), **b.** single element model (SE), and **c.** exact test geometry (ETG).

MP model is created in MATLAB[®], and simulations are performed for uni-axial axis-symmetric deformation gradient, Equation (40).

$$\mathbf{F} = \begin{bmatrix} \exp(\dot{\epsilon}_0 t) & 0 & 0 \\ 0 & \exp(-0.5\dot{\epsilon}_0 t) & 0 \\ 0 & 0 & \exp(-0.5\dot{\epsilon}_0 t) \end{bmatrix} \quad (40)$$

Initial crystal orientation, \mathbf{g} , is computed by using the axial loading (tension or compression) direction (hkl) and assuming a transverse direction $[uvw]$ normal to it using Equation (41).

$$\mathbf{g} = \begin{bmatrix} h & p & u \\ k & q & v \\ l & r & w \end{bmatrix} \quad (41)$$

Crystal based dislocation density based constitutive relations is incorporated to a commercial finite element software (MSC MARC[®]) through its user-subroutine (HYPELA2) to define general material rules. Finite element model is then used to simulate two different models; single element (SE) and exact test geometry (ETG). ETG model represents one-quarter of an exact test geometry of a sample in accordance with EN ISO 6892-1 standard. ETG model consists of 232 finite elements.

Finite element models for Single Element (SE) and Exact Test Geometry (ETG) have

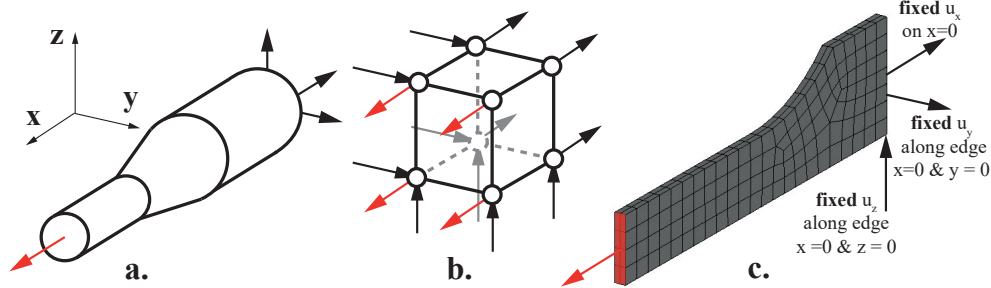


Figure 3: Boundary conditions for **a.** MP model, **b.** SE model, and **c.** ETG model. Red arrows indicate specified displacements while black arrows indicate the fixed displacements.

the following properties. Hexahedral linear elements with eight nodes per element are used. Boundary conditions are selected to get a uni-axial strain state throughout the sample, Figure 3. Overall engineering stress is calculated by summation all of the reaction forces along the axial direction (x-direction) at the gauge cross-section of the sample and then dividing the total result by undeformed (initial) area. Strains are computed by normalizing the given displacements by gauge length.

To establish consistency between the results from the experimental and numerical references and our simulations the calibrations were conducted. For this purpose first the effects of each multiplier on the stress-strain curves were understood through trial runs. Then several trial runs were attempted using different values as the calibrators. The calibration was done with keeping the parameters within specific and reasonable ranges to avoid drastic shifts among the case studies. Eventually the sets which had been giving best matches between the simulation and reference results were picked and reported.

3. Results and Discussion

The proposed model is applied to explain different experimental findings for single crystals of α -iron and dependence of its mechanical response on crystal orientation, temperature, strain-rate were investigated. Tension-Compression asymmetry and flow stresses were also

computed using the proposed physics based model. Experimental data from the literature is used to support the numerical findings. Therefore, different calibration constants for various experimental data sets are used in literature, Appendix 6.1.

3.1. Crystal orientation

Crystal orientation changes the mechanical response significantly for bcc materials. Keh studied crystal orientation dependence of single crystal behavior for α -iron [5] up to 5% strain approximately at room temperature. Table 4 shows the experimental test conditions in the corresponding reference [5].

Table 4: Experimental test cases used for crystal orientation dependence of α -iron in the reference [5].

temperature [K]	strain rate [1/s]	loading directions	load type
298	3.3×10^{-4}	[001], [011], $[\bar{1}11]$	tension

Calibration of the proposed model at different scales (MP, SE, and ETG) were performed to get the best fits to the experimental data as shown in Table 10. Figure 4 shows three stress-strain graphs for three different crystallographic directions of [0 0 1], [0 1 1], and $[\bar{1} 1 1]$ as used in the reference [5]. Lowest strain hardening rate was present along [0 1 1] direction while the highest strain hardening was obtained for $[\bar{1} 1 1]$ tensile direction as in the experimental findings.

The forest projection operator in Equation (12) and dislocation interaction matrix in Equation (34) are the two effective factors in the model to replicate the orientation dependence. The experiments were performed nearly at room temperature [5] hence a limited effect of non-Schmid terms are expected. The source of the anisotropy relies on the strain hardening interactions between slip systems. The forest projection operator that is used in

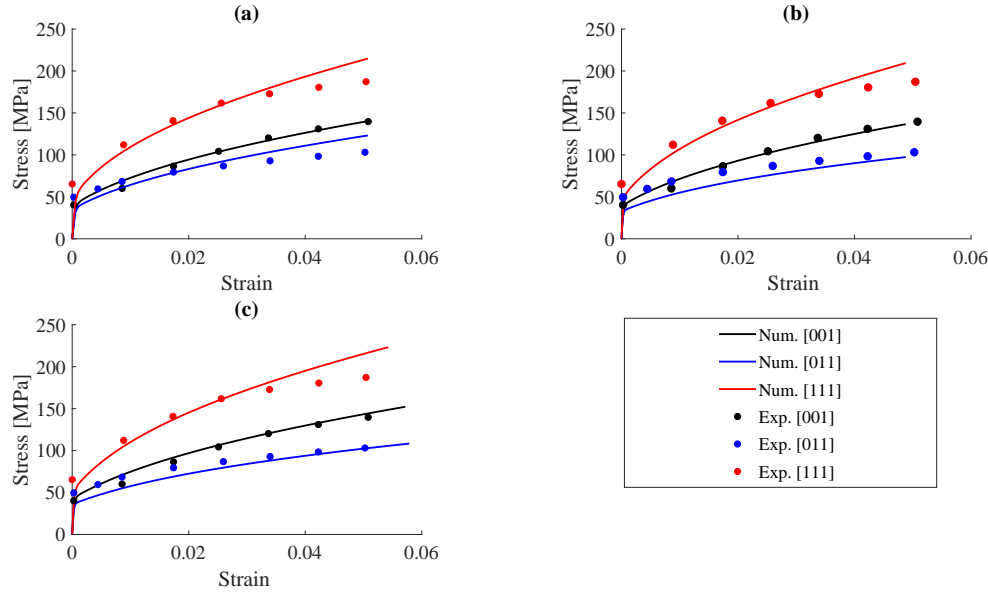


Figure 4: Dependence of the stress-strain on the crystal orientation under tensile loading for different model scales: **a.** MP, **b.** SE, and **c.** ETG. Experimental data belongs to [5].

this study is very essential part of this proposed strain hardening or dislocation evolution scheme.

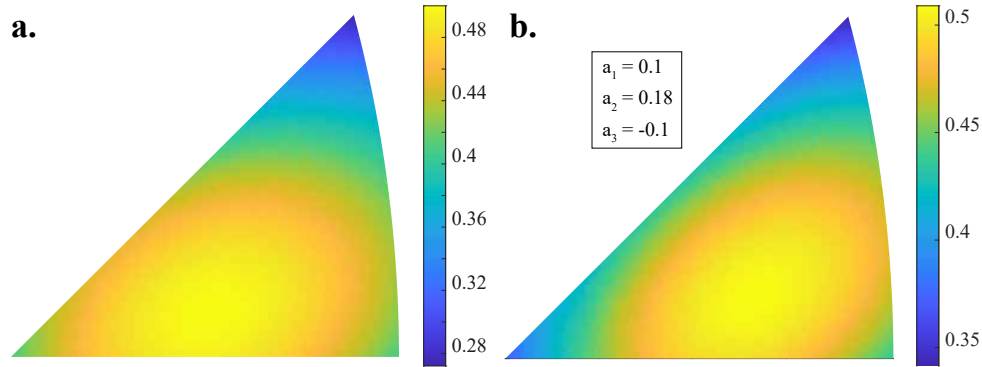


Figure 5: Distribution of maximum **a.** resolved shear stress (τ^α) and **b.** cumulative resolved shear stress including non-Schmid projections ($\tau^\alpha + \sigma_{ns}^\alpha$) for tensile loading. Values of Non-Schmid constants are indicated.

In all of the graphs a reasonable match with the experimental results was obtained after a tedious calibration procedure. The parameters that are used for calibrating the MP, SE and ETG models are presented in Table 10. Among the results, the capability of the MP

model in catching the experimental deformation pattern was slightly better than the other model scales in terms of hardening rate and yield behavior. This can be attributed to the numerical errors in the finite element models and averaging of the nodes to a proper measure for the stress. The results of the finite element models needs to be post-processed that makes calibration more exhausting. Therefore, easy calibration and faster response of MP model makes it a preferred model scale for modeling simple deformation states just like the uni-axial strain state as in the current case.

Figure 5.a displays the maximum resolved shear stress distribution. According to the contour plot and the color bar, the minimum Schmid factor among $[0\ 0\ 1]$, $[0\ 1\ 1]$, $[\bar{1}\ 1\ 1]$ orientations is along $[\bar{1}\ 1\ 1]$ crystal direction. This causes the flow stress to be highest if the crystal were tensile loaded along $[\bar{1}\ 1\ 1]$ direction. The other two orientations have little or no difference at room temperature as in the experiments [5].

Figure 5 b. shows the effect of Non-Schmid effects for non-Schmid factors of a_1 , a_2 , a_3 of 0.1, 0.18, and -0.1 were used for a uni-axial tensile loading case. Non-Schmid terms allow variation of the yield magnitudes for different orientations. In this case, yield is expected to occur at a higher stress magnitude for tensile direction of $[0\ 0\ 1]$ or cube orientation, than that of $[\bar{1}\ 1\ 1]$ or $[0\ 0\ 1]$ orientation. Because the maximum resolved cumulative shear factor is lower for $[0\ 0\ 1]$ direction than $[0\ 1\ 1]$ direction. However, there is also the effect of strain hardening which can not be overlooked.

The effect of interaction coefficients analogous as latent hardening coefficients on crystal orientation dependence for bcc materials is also investigated. Different hardening coefficients than Franciosi constants in Equation (34) were used and a much better correlation was obtained as shown in Figure 6. Early yield of cube orientation, that were present in the experimental data can also be replicated considering the proportional limit to identify the yield stresses.

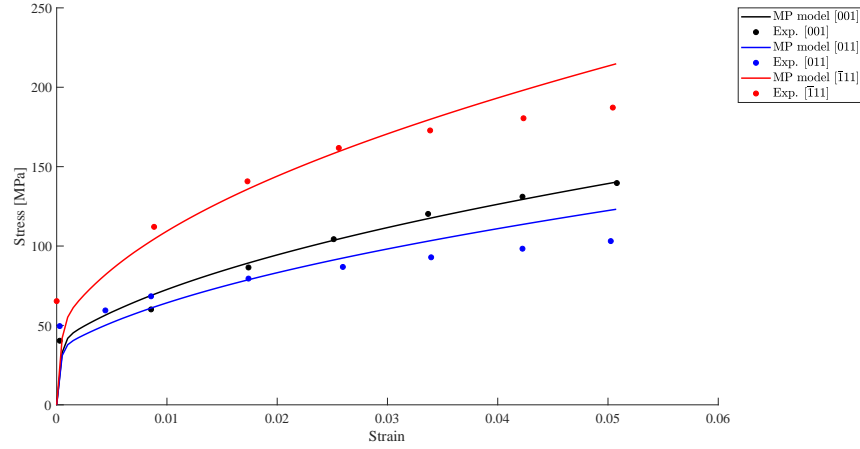


Figure 6: Crystal orientation effect for α -iron by calibration of hardening interaction coefficients, experimental data from [5].

3.2. Temperature

Temperature dependence of the model was incorporated using Peierls activation energy barrier in the proposed modeling scheme through Equation (15). The model was used to validate two different experimental findings for tension and compression cases, separately.

Temperature dependence of mechanical response of single crystals α -iron was studied experimentally by Spitzig and Keh [70]. Tensile experiments were performed at temperatures of 143 K, 195 K, 250 K and 295 K. Table 5 shows the experimental test cases of Spitzig and Keh [70].

Table 5: Experimental test cases used for temperature dependence of α -iron in the reference [70].

temperatures [K]	strain rate [1/s]	loading direction	load type
143, 195, 250, 295	5.6×10^{-4}	[149]	tension

Calibration of model constants were performed for different modeling scales (MP, SE, and ETG), Table 11. Figure 7 shows simulation results together with the experimental findings [70]. A quite well match between the model results and experimental findings were obtained.

The model reveals a very good correlation with the experimental curves for the temperature dependence at all of the model scales. As the temperature decreases, mechanical strength increases as expected. Thermal activation concept to overcome Peierls barrier governs the physics of plastic flow in bcc metals hence revealing a good correlation of the mechanical response (flow stress) with temperatures.

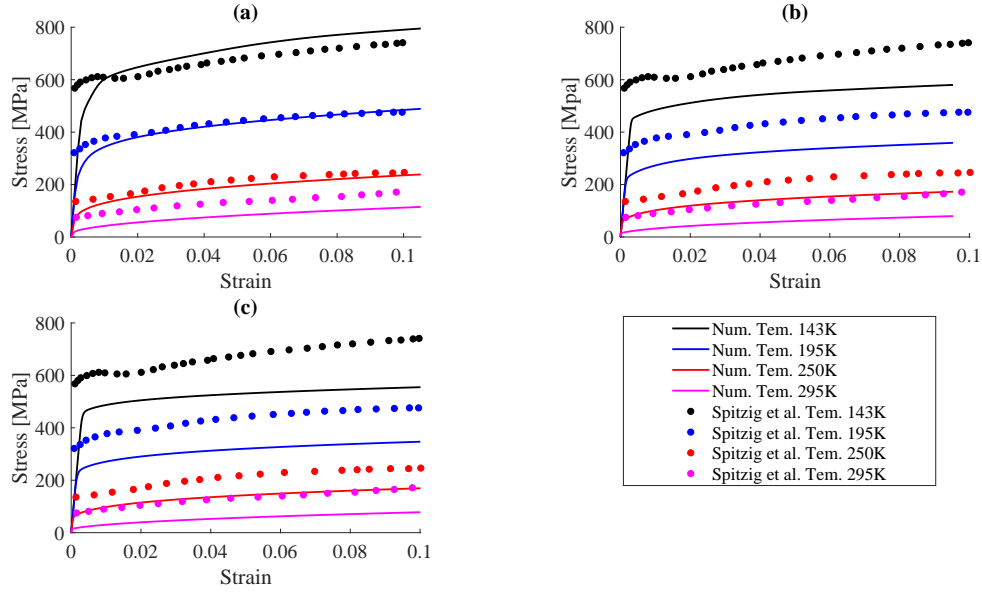


Figure 7: Dependence of the stress-strain graphs on the temperature for **a.** MP, **b.** SE, **c.** ETG models and comparison to the experimental data [70].

The effect of temperature on yield stress of single crystals of α -iron was also investigated and compared to the same reference [70]. In the experiments tensile tests were performed along three different crystallographic directions were loaded at four temperature levels.

Figure 8 shows the comparison of yield stress results that were computed using our MP model both with experimental tests reported by Spitzig and Keh [70], and numerical study done by Patra and McDowell [54]. The calculated yield stresses has a discrepancy with respect to the experimental results. The proposed model at MP scale agrees as well a different model in the literature [54] that takes into account the temperature of non-Schmid effects using a rigorous model. At all temperatures, the experimental yield stresses were

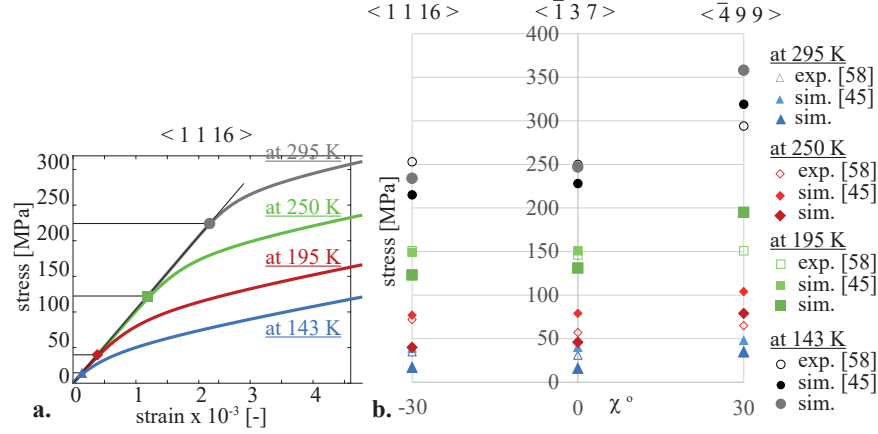


Figure 8: Dependence of the flow stress on the temperature and crystal orientation: **a.** computation of flow stress for $[1\ 1\ 16]$ tensile direction, **b.** flow stress results for three different tensile directions of $[1\ 1\ 16]$, $[1\ 3\ 7]$, $[4\ 9\ 9]$ and at four different temperatures of 143 K, 195 K, 250 K, and 295 K. χ denotes the offset from the single slip orientation, $[1\ 3\ 7]$.

under-predicted for tensile direction of $[1\ 1\ 16]$ while they were over-predicted for tensile direction of $[4\ 9\ 9]$ by the proposed modeling scheme. The major difference is related to the use of the same constants for non-Schmid effects at different temperatures. It is well known that the non-Schmid effects decays as temperature increases. For this reason, the flow stress is overestimated at room temperatures causing the mismatch from the experimental findings.

Temperature dependent compression experiments were conducted on α -iron single crystals by Zwiese and Diehl [71] for the experimental conditions in Table 6. Calibration was performed and model constants were obtained as shown in Table 10.

Table 6: Experimental test cases used for temperature dependence of α -iron in the reference [71].

temperatures [K]	strain rate [1/s]	load direction	load type
77, 90, 160, 196, 210, 270, 295, 360, 410	5.6×10^{-4}	[0.266 0.492 0.829]	compression

Figure 9 shows the results for three different modeling scales after calibration and their comparison to the experimental stress-strain response. The strain hardening response was in

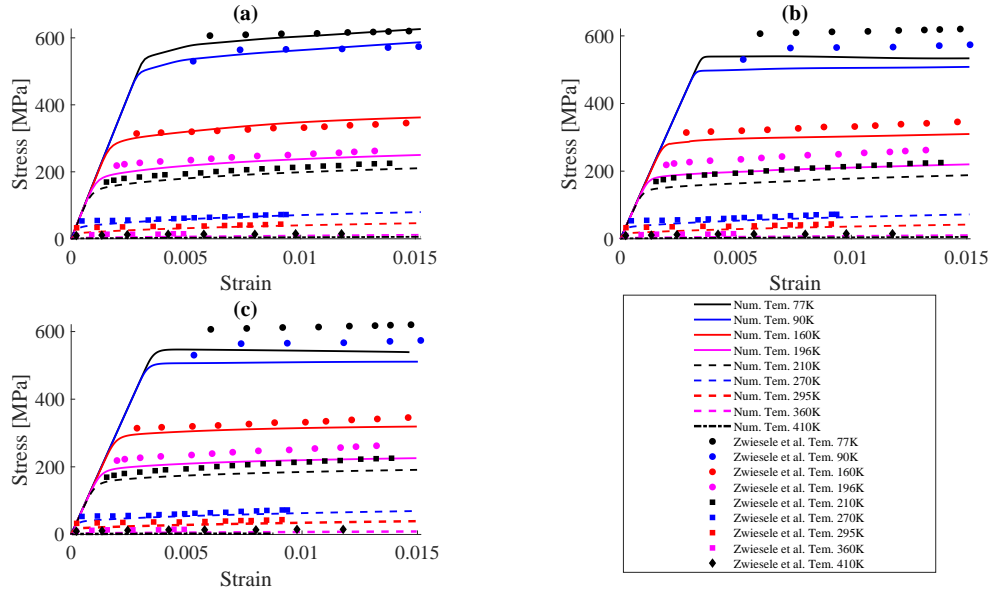


Figure 9: Dependence of the stress-strain graphs on the temperature for **a.** MP, **b.** SE, **c.** ETG models and comparison to the experimental data [71].

slightly better agreement with the experiments for MP model scale. Temperature dependence of yield stress and strain hardening response can be captured with the proposed model.

3.3. Strain-rate

The proposed model was used to simulate the strain rate dependence of mechanical response of α -iron single crystal. The stress-strain coupling that is used within the proposed model is not a simple relationship. Slip-rate is governed by Orowan law which is a function of both the mobile dislocations and dislocation velocity. Mobile dislocation density is computed using a function of effective stress while dislocation velocity is governed by the dominant exponential law, Equation (15). Therefore, the proposed model has inherent dependence on strain rate that is not as direct as power-law that was commonly used to find slip rates.

Table 7 shows the strain rates that were used in reference [72]. Figure 10 shows the resultant engineering stress-strain curves of the different model scales. Model constants that were employed to calibrate the results are shown in Table 11.

Table 7: Numerical test cases used for strain rate dependence of α -iron in the reference [72].

temperature [K]	strain rates [1/s]	load direction	load type
300	3.3×10^{-4} , 3.3×10^{-3} , 3.3×10^{-2}	[100]	tension

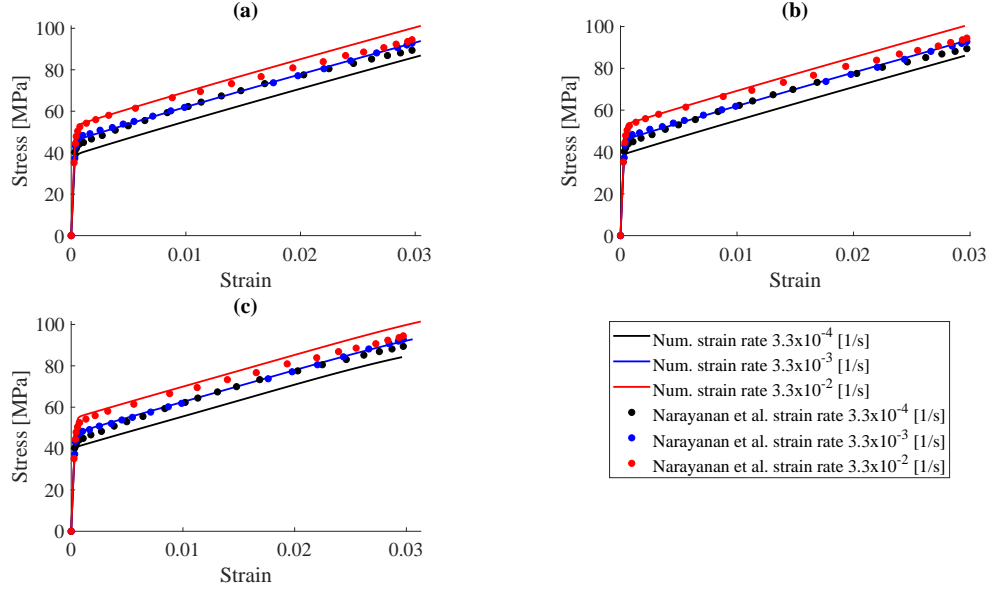
Figure 10: Stress-strain curves for different strain rates of **a.** MP, **b.** SE, **c.** ETG models and comparison to the reference [72].

Figure 10 shows the results for three different strain rates. All of the models match well the strain rate dependency of the reference data. A relatively better agreement of the MP model curves with the reference graphs was noted.

Similarly, the presented model is employed to simulate the strain-rate dependence of mechanical response of a different reference [73]. The modeling inputs are presented in Table 8. Model constants that were calibrated are tabulated in Table 11.

Table 8: Numerical test cases used for strain rate dependence of α -iron in the reference [73].

temperature [K]	strain rates [1/s]	load direction	load type
300	1.0×10^{-4} , 1.0×10^{-2} , 1.0	[149]	tension

Figure 11 shows the results of the proposed model and reference data from [73]. The reference data had significant difference for various levels of strain rates, hence this analysis shows better the relative match of the stress-strain response. MP model matches well the strain-rate dependence of the single crystals of α -iron single crystals. The results of the other modeling scales also provide a reasonable match with the reference.

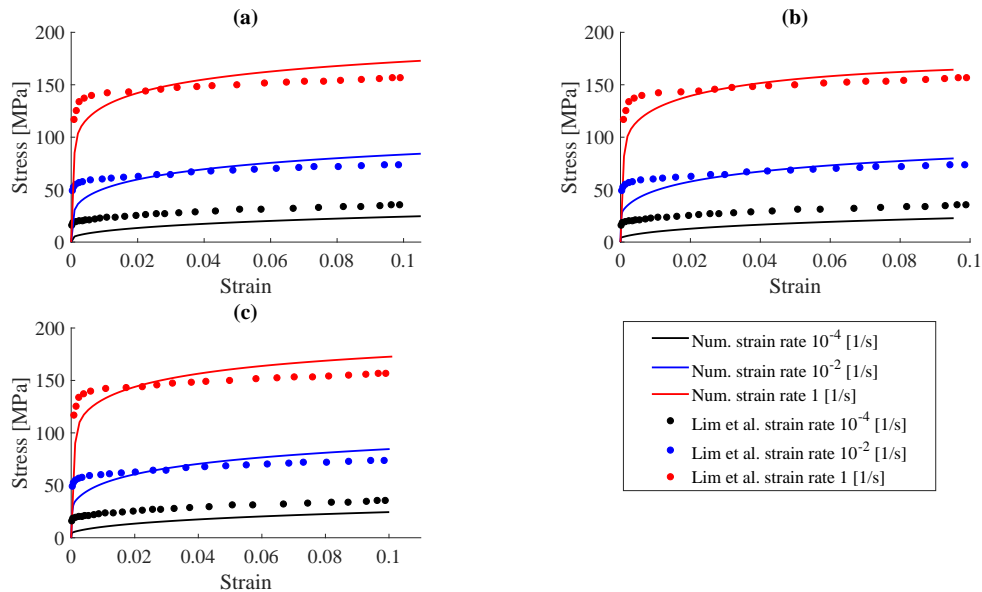


Figure 11: Stress-strain curves for strain rates using different model scales of **a.** MP, **b.** SE, **c.** ETG models and comparison to the reference [73].

3.4. Tension-Compression asymmetry

The asymmetry in the tension/compression response of the α -iron has been experimentally investigated by Zwiese and Diehl [71]. They have conducted tension and compression tests at different temperature levels on the single crystal samples whose orientations were quite stereographically close. The experiments are reported in the form of flow stress versus temperature.

Table 9: Experimental test cases used for tension-compression asymmetry of α -iron in the reference [71]

temperatures [K]	strain rate $\dot{\epsilon}$ (1/s)	load direction	load type
50, 100, 150, 200, 250, 300, 350, and 400	5.6×10^{-4}	$[-0.282 \ 0.511 \ 0.811]$	tension
		$[-0.309 \ 0.462 \ 0.830]$	tension
		$[-0.266 \ 0.460 \ 0.847]$	compression
		$[-0.277 \ 0.494 \ 0.824]$	compression

The proposed model was used to simulate the yield stress of the iron single crystal under compressive and tensile loading modes. The models are calibrated based on the experimental results. The strain rate value, crystal orientation, total deformation and temperature in the simulations are set up in such a way to promote the conditions that are experimentally established by Zwieseles and Diehl [71]. The simulation conditions are provided in Table 9. Model constants were calibrated using the values in Table 11.

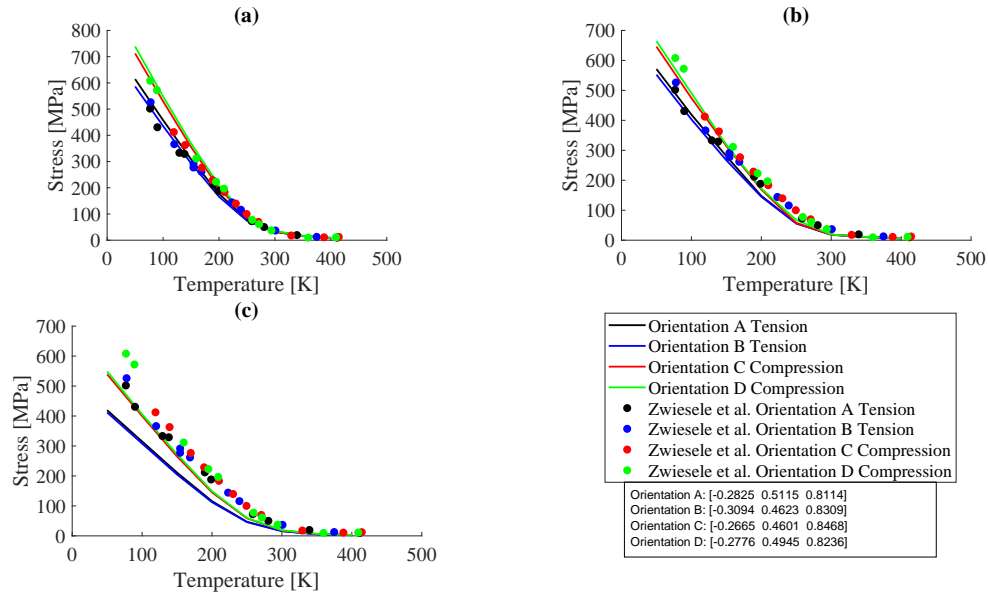
Figure 12: Comparison of simulated tension/compression asymmetry in α -iron single crystals at different temperatures for different model scales of **a.** MP, **b.** SE, **c.** ETG, together with experimental findings [71]

Figure 12 shows the model findings together with the experimental data from [71]. All of the model scales were capable to simulate the asymmetric behavior of tension/compression response. However, among the presented models, the best fit is achieved using the SE model.

The proposed modeling scheme did not use the temperature dependent non-Schmid constants, hence this gives rise to the difference in the estimated values of the flow stress. Even though a simple modeling approach used, it was possible to replicate the tension/compression asymmetry of stress-strain curves.

4. Conclusions

In this work, a physically based model was developed and applied to simulate various literature findings for single crystals of α -iron. The model well captures the general mechanical response of bcc materials.

- Forest projection term, that uses the slip plane normal of slip systems, interaction coefficients, and dislocation density based evolution model are the key features to capture crystal orientation dependence of bcc materials. The proposed model well represents the experimental crystal orientation dependence of α -iron [5] by incorporating those features.
- Thermally activated slip based on Peierls activation energy provides inherent dependence of the model on temperature to correlate mechanical response of bcc metals with temperature. Therefore, proposed model well matches the experimental findings temperature dependence of single crystal α -iron [70, 71].
- Calibration can be performed easily for MP model scale than the finite element models because simulations take longer and results shall be post-processed for finite element models. Finite element models are recommended when deviations from the ideal boundary conditions are expected.

Proposed model will be used to simulate polycrystal response of a bcc alloy that contains α -ferrite particles. Therefore, it is very important to develop a model that is as simple as

possible but that can represent temperature, strain-rate, crystal orientation dependence of a bcc material.

5. Acknowledgement

Authors greatly acknowledge the funding from The Scientific and Technological Research Council of Turkey (TUBITAK) - The Scientific and Technological Research Projects Funding Program (1001) under grant number 118M285.

6. Appendix

6.1. Model constants

Table 10 shows the model constants used for the three different model scales; material point (MP), single finite element (SE), and exact tensile geometry (ETG) that were calibrated for different experimental findings in the references for crystal orientation dependence [5] and temperature dependence [70, 71].

Table 11 shows the calibrated model constants used for the three different model scales; material point (MP), single finite element (SE), and exact tensile geometry (ETG) for strain-rate [73, 72] and tension-compression asymmetry [71].

Table 10: Description and values of constants for orientation dependence case study of Keh [5]

<u>const.</u>	<u>ori. dep. [5]</u> All models	<u>temp. dep. [70]</u> All models	<u>temp. dep. [71]</u> All models
c_1	0.2	0.03	0.03
c_2	7	11	11
c_3	10	9	9
c_4	0.006	0.03	0.03
c_5	10	10	10
c_6	1000	1000	1000
c_7	0.1	0.1	0.1
c_8	0.08	0.08	0.08
a_1	0.02	0.1	0.65
a_2	-0.02	0.02	0.1
a_3	-0.58	0.1	-0.45
ϱ^0	1×10^{10}	1×10^{11}	1×10^{11}
$Q_{Pei}(\times 10^{-19})$	1.009	0.881	0.929

References

[1] C. Hamelin, B. Diak, A. Pilkey, Multiscale modelling of the induced plastic anisotropy in bcc metals, International Journal of Plasticity 27 (8) (2011) 1185–1202.

[2] A. Patra, D. L. McDowell, Crystal plasticity-based constitutive modelling of irradiated bcc structures, Philosophical Magazine 92 (7) (2012) 861–887.

[3] M. Knezevic, I. J. Beyerlein, M. L. Lovato, C. N. Tomé, A. W. Richards, R. J. McCabe, A strain-rate and temperature dependent constitutive model for bcc metals incorporating non-schmid effects: application to tantalum–tungsten alloys, International Journal of Plasticity 62 (2014) 93–104.

[4] G. Gottstein, Physical foundations of materials science, Springer Science & Business

Table 11: Description and values of constants for strain rate dependence study of Lim [73]

<u>const.</u>	<u>rate dep. [73]</u> All models	<u>rate dep. [72]</u> All models	<u>TC asym. [71]</u> All models
c_1	0.001	0.03	0.1
c_2	15	1	1
c_3	24	155	16
c_4	0.03	0.02	0.1
c_5	10	10	10
c_6	1000	1000	1000
c_7	0.1	0.1	0.1
c_8	0.08	0.08	0.08
a_1	0.08	0.08	0.35
a_2	0.02	0.001	-0.4
a_3	-0.5	-0.0002	0.34
ρ^0	1×10^{11}	1×10^{12}	1×10^{10}
$Q_{Pei}(\times 10^{-19})$	0.865	1.041	0.865
Media, 2013.			

- [5] A. Keh, Work hardening and deformation sub-structure in iron single crystals deformed in tension at 298 k, Philosophical Magazine 12 (115) (1965) 9–30.
- [6] F. Guiu, P. Pratt, The effect of orientation on the yielding and flow of molybdenum single crystals, physica status solidi (b) 15 (2) (1966) 539–552.
- [7] S. Takeuchi, K. Maeda, Slip in high purity tantalum between 0.7 and 40 k, Acta metallurgica 25 (12) (1977) 1485–1490.
- [8] J. Nagakawa, M. Meshii, The deformation of niobium single crystals at temperatures between 77 and 4.2 k, Philosophical Magazine A 44 (5) (1981) 1165–1191.

- [9] W. Wasserbäch, Anomalous slip in high-purity niobium and tantalum single crystals, *Physica status solidi (a)* 147 (2) (1995) 417–446.
- [10] A. Seeger, W. Wasserbäch, Anomalous slip—a feature of high-purity body-centred cubic metals, *physica status solidi (a)* 189 (1) (2002) 27–50.
- [11] E. Kuramoto, Y. Aono, K. Kitajima, Thermally activated slip deformation of high purity iron single crystals between 4.2 k and 300 k, *Scripta Metallurgica* 13 (11) (1979) 1039–1042.
- [12] D. Caillard, Kinetics of dislocations in pure fe. part i. in situ straining experiments at room temperature, *Acta Materialia* 58 (9) (2010) 3493–3503.
- [13] M. Tang, L. Kubin, G. Canova, Dislocation mobility and the mechanical response of bcc single crystals: a mesoscopic approach, *Acta Materialia* 46 (9) (1998) 3221–3235.
- [14] Y. Aono, E. Kuramoto, K. Kitajima, Fundamental plastic behaviors in high-purity bcc metals (nb, mo and fe), in: *Strength of Metals and Alloys (ICSMA 6)*, Elsevier, 1982, pp. 9–14.
- [15] A. Argon, *Strengthening mechanisms in crystal plasticity*, Vol. 4, Oxford University Press on Demand, 2008.
- [16] A. Ma, F. Roters, D. Raabe, A dislocation density based constitutive law for bcc materials in crystal plasticity fem, *Computational Materials Science* 39 (1) (2007) 91 – 95, proceedings of the 15th International Workshop on Computational Mechanics of Materials.
- [17] C. R. Weinberger, C. C. Battaile, T. E. Buchheit, E. A. Holm, Incorporating atomistic data of lattice friction into bcc crystal plasticity models, *International Journal of Plasticity* 37 (2012) 16–30.

- [18] J. Christian, Some surprising features of the plastic deformation of body-centered cubic metals and alloys, *Metallurgical transactions A* 14 (7) (1983) 1237–1256.
- [19] E. Schmid, W. Boas, *Plasticity of crystals*, London, 1950.
- [20] A. S. Khan, R. Liang, Behaviors of three bcc metal over a wide range of strain rates and temperatures: experiments and modeling, *International Journal of Plasticity* 15 (10) (1999) 1089–1109.
- [21] G. Z. Voyiadjis, F. H. Abed, A coupled temperature and strain rate dependent yield function for dynamic deformations of bcc metals, *International Journal of Plasticity* 22 (8) (2006) 1398–1431.
- [22] P. Jeffcoat, B. Mordike, K. Rogausch, Anomalous slip in mo-5 at.% nb and mo-5 at.% re alloy single crystals, *The Philosophical Magazine: A Journal of Theoretical Experimental and Applied Physics* 34 (4) (1976) 583–592.
- [23] H. Matsui, H. Kimura, Anomalous {110} slip in high-purity molybdenum single crystals and its comparison with that in v (a) metals, *Materials Science and Engineering* 24 (2) (1976) 247–256.
- [24] M. Duesbery, R. Foxall, A detailed study of the deformation of high purity niobium single crystals, *Philosophical Magazine* 20 (166) (1969) 719–751.
- [25] C. Bolton, G. Taylor, Anomalous slip in high-purity niobium single crystals deformed at 77 k in tension, *Philosophical Magazine* 26 (6) (1972) 1359–1376.
- [26] V. Vitek, M. Mrovec, R. Gröger, J. Bassani, V. Racherla, L. Yin, Effects of non-glide stresses on the plastic flow of single and polycrystals of molybdenum, *Materials Science and Engineering: A* 387 (2004) 138–142.

- [27] V. Vitek, V. Paidar, Non-planar dislocation cores: a ubiquitous phenomenon affecting mechanical properties of crystalline materials, *Dislocations in solids* 14 (2008) 439–514.
- [28] L. Kubin, The low temperature mechanical properties of bcc metals and their alloys, *Reviews on the deformation behavior of materials* 4 (3) (1982) 181–275.
- [29] M. Duesbery, On non-glide stresses and their influence on the screw dislocation core in body-centred cubic metals i. the peierls stress, *Proceedings of the Royal Society of London. A. Mathematical and Physical Sciences* 392 (1802) (1984) 145–173.
- [30] M. a.-S. Duesbery, V. Vitek, Plastic anisotropy in bcc transition metals, *Acta Materialia* 46 (5) (1998) 1481–1492.
- [31] V. Vitek, Structure of dislocation cores in metallic materials and its impact on their plastic behaviour, *Progress in materials science* 36 (1992) 1–27.
- [32] K. Ito, V. Vitek, Atomistic study of non-schmid effects in the plastic yielding of bcc metals, *Philosophical Magazine A* 81 (5) (2001) 1387–1407.
- [33] Z. Wang, I. Beyerlein, An atomistically-informed dislocation dynamics model for the plastic anisotropy and tension–compression asymmetry of bcc metals, *International Journal of Plasticity* 27 (10) (2011) 1471–1484.
- [34] A. Koester, A. Ma, A. Hartmaier, Atomistically informed crystal plasticity model for body-centered cubic iron, *Acta Materialia* 60 (9) (2012) 3894–3901.
- [35] R. Gröger, V. Vitek, Impact of non-schmid stress components present in the yield criterion for bcc metals on the activity of $\{110\}_I$ 111_L slip systems, *Computational Materials Science* 159 (2019) 297–305.

- [36] H. Cho, C. A. Bronkhorst, H. M. Mourad, J. R. Mayeur, D. Luscher, Anomalous plasticity of body-centered-cubic crystals with non-schmid effect, *International Journal of Solids and Structures* 139 (2018) 138–149.
- [37] A. Arsenlis, M. Tang, Simulations on the growth of dislocation density during stage 0 deformation in bcc metals, *Modelling and Simulation in Materials Science and Engineering* 11 (2) (2003) 251.
- [38] A. Patra, D. L. McDowell, Continuum modeling of localized deformation in irradiated bcc materials, *Journal of Nuclear Materials* 432 (1-3) (2013) 414–427.
- [39] H. Li, X. Sun, H. Yang, A three-dimensional cellular automata-crystal plasticity finite element model for predicting the multiscale interaction among heterogeneous deformation, drx microstructural evolution and mechanical responses in titanium alloys, *International Journal of Plasticity* 87 (2016) 154–180.
- [40] L. Stainier, A. M. Cuitiño, M. Ortiz, A micromechanical model of hardening, rate sensitivity and thermal softening in bcc single crystals, *Journal of the Mechanics and Physics of Solids* 50 (7) (2002) 1511–1545.
- [41] Y. J. Lee, G. Subhash, G. Ravichandran, Constitutive modeling of textured body-centered-cubic (bcc) polycrystals, *International Journal of Plasticity* 15 (6) (1999) 625–645.
- [42] M. Lee, H. Lim, B. Adams, J. Hirth, R. Wagoner, A dislocation density-based single crystal constitutive equation, *International Journal of Plasticity* 26 (7) (2010) 925–938.
- [43] R. A. Austin, D. L. McDowell, A dislocation-based constitutive model for viscoplastic deformation of fcc metals at very high strain rates, *International Journal of Plasticity* 27 (1) (2011) 1–24.

[44] M. Ardeljan, I. J. Beyerlein, M. Knezevic, A dislocation density based crystal plasticity finite element model: application to a two-phase polycrystalline hcp/bcc composites, *Journal of the Mechanics and Physics of Solids* 66 (2014) 16–31.

[45] A. Arsenlis, D. M. Parks, Modeling the evolution of crystallographic dislocation density in crystal plasticity, *Journal of the Mechanics and Physics of Solids* 50 (9) (2002) 1979–2009.

[46] A. Ma, F. Roters, A constitutive model for fcc single crystals based on dislocation densities and its application to uniaxial compression of aluminium single crystals, *Acta materialia* 52 (12) (2004) 3603–3612.

[47] E. Demir, A physically based constitutive model for fcc single crystals with a single state variable per slip system, *Modelling and Simulation in Materials Science and Engineering* 25 (1) (2016) 015009.

[48] E. Demir, I. Gutierrez-Urrutia, Investigation of strain hardening near grain boundaries of an aluminum oligocrystal: Experiments and crystal based finite element method, *International Journal of Plasticity* (2020) 102898.

[49] Q. Qin, J. L. Bassani, Non-schmid yield behavior in single crystals, *Journal of the Mechanics and Physics of Solids* 40 (4) (1992) 813–833.

[50] Q. Qin, J. L. Bassani, Non-associated plastic flow in single crystals, *Journal of the Mechanics and Physics of Solids* 40 (4) (1992) 835–862.

[51] P. Steinmann, E. Kuhl, E. Stein, Aspects of non-associated single crystal plasticity: influence of non-schmid effects and localization analysis, *International journal of solids and structures* 35 (33) (1998) 4437–4456.

- [52] S. Nemat-Nasser, T. Okinaka, L. Ni, A physically-based constitutive model for bcc crystals with application to polycrystalline tantalum, *Journal of the Mechanics and Physics of Solids* 46 (6) (1998) 1009–1038.
- [53] T. Yalcinkaya, W. Brekelmans, M. Geers, Bcc single crystal plasticity modeling and its experimental identification, *Modelling and Simulation in Materials Science and Engineering* 16 (8) (2008) 085007.
- [54] A. Patra, T. Zhu, D. L. McDowell, Constitutive equations for modeling non-schmid effects in single crystal bcc-fe at low and ambient temperatures, *International Journal of Plasticity* 59 (2014) 1–14.
- [55] D. J. Savage, I. J. Beyerlein, M. Knezevic, Coupled texture and non-schmid effects on yield surfaces of body-centered cubic polycrystals predicted by a crystal plasticity finite element approach, *International Journal of Solids and Structures* 109 (2017) 22–32.
- [56] E. H. Lee, Elastic-plastic deformation at finite strains, Technical Report (1969).
- [57] G. Po, Y. Cui, D. Rivera, D. Cereceda, T. D. Swinburne, J. Marian, N. Ghoniem, A phenomenological dislocation mobility law for bcc metals, *Acta Materialia* 119 (2016) 123–135.
- [58] A. Maniatty, P. Dawson, Y.-S. Lee, A time integration algorithm for elasto-viscoplastic cubic crystals applied to modelling polycrystalline deformation, *International Journal for Numerical Methods in Engineering* 35 (8) (1992) 1565–1588.
- [59] S. R. Kalidindi, C. A. Bronkhorst, L. Anand, Crystallographic texture evolution in bulk deformation processing of fcc metals, *Journal of the Mechanics and Physics of Solids* 40 (3) (1992) 537–569.

[60] E. Demir, F. Roters, D. Raabe, Bending of single crystal microcantilever beams of cube orientation: Finite element model and experiments, *Journal of the Mechanics and Physics of Solids* 58 (10) (2010) 1599–1612.

[61] F. Roters, D. Raabe, G. Gottstein, Work hardening in heterogeneous alloy - a microstructural approach based on three internal state variables, *Acta materialia* 48 (17) (2000) 4181–4189.

[62] U. Kocks, H. Mecking, Physics and phenomenology of strain hardening: the fcc case, *Progress in materials science* 48 (3) (2003) 171–273.

[63] H. J. Frost, M. F. Ashby, Deformation mechanism maps: the plasticity and creep of metals and ceramics, Pergamon press, 1982.

[64] M. Geers, M. Cottura, B. Appolaire, E. P. Busso, S. Forest, A. Villani, Coupled glide-climb diffusion-enhanced crystal plasticity, *Journal of the Mechanics and Physics of Solids* 70 (2014) 136–153.

[65] E. Nes, Modelling of work hardening and stress saturation in fcc metals, *Progress in materials science* 41 (3) (1997) 129–193.

[66] P. Franciosi, Glide mechanisms in bcc crystals: an investigation of the case of α -iron through multislip and latent hardening tests, *Acta Metallurgica* 31 (9) (1983) 1331–1342.

[67] J. J. Adams, D. Agosta, R. Leisure, H. Ledbetter, Elastic constants of monocrystal iron from 3 to 500 k, *Journal of applied physics* 100 (11) (2006) 113530.

[68] R. Johnson, D. Oh, Analytic embedded atom method model for bcc metals, *Journal of Materials Research* 4 (5) (1989) 1195–1201.

- [69] A. Das, Revisiting stacking fault energy of steels, *Metallurgical and Materials Transactions A* 47 (2) (2016) 748–768.
- [70] W. Spitzig, A. Keh, Orientation and temperature dependence of slip in iron single crystals, *Metallurgical Transactions* 1 (10) (1970) 2751.
- [71] S. Zwieselee, J. Diehl, Temperature and strain rate dependence of the macro yield stress of high purity iron single crystals, in: *Strength of Metals and Alloys*, Elsevier, 1979, pp. 59–64.
- [72] S. Narayanan, D. L. McDowell, T. Zhu, Crystal plasticity model for bcc iron atomistically informed by kinetics of correlated kinkpair nucleation on screw dislocation, *Journal of the Mechanics and Physics of Solids* 65 (2014) 54–68.
- [73] H. Lim, L. Hale, J. Zimmerman, C. Battaile, C. Weinberger, A multi-scale model of dislocation plasticity in α -Fe: Incorporating temperature, strain rate and non-schmid effects, *International Journal of Plasticity* 73 (2015) 100–118.